

See discussions, stats, and author profiles for this publication at: <https://www.researchgate.net/publication/40893573>

# Oxidation and Reduction Products of X Irradiation at 10 K in Sucrose Single Crystals: Radical Identification by EPR, ENDOR, and DFT

ARTICLE in THE JOURNAL OF PHYSICAL CHEMISTRY B · JANUARY 2010

Impact Factor: 3.3 · DOI: 10.1021/jp909247z · Source: PubMed

CITATIONS

11

READS

19

6 AUTHORS, INCLUDING:



[Ewald Pauwels](#)

Ghent University

56 PUBLICATIONS 666 CITATIONS

[SEE PROFILE](#)



[Henk Vrielinck](#)

Ghent University

111 PUBLICATIONS 827 CITATIONS

[SEE PROFILE](#)



[Einar Sagstuen](#)

University of Oslo

176 PUBLICATIONS 2,399 CITATIONS

[SEE PROFILE](#)



[Michel Waroquier](#)

Ghent University

417 PUBLICATIONS 8,266 CITATIONS

[SEE PROFILE](#)

# Oxidation and Reduction Products of X Irradiation at 10 K in Sucrose Single Crystals: Radical Identification by EPR, ENDOR, and DFT

Hendrik De Cooman,<sup>†,‡</sup> Ewald Pauwels,<sup>‡</sup> Henk Vrielinck,<sup>†</sup> Einar Sagstuen,<sup>§</sup> Michel Waroquier,<sup>‡</sup> and Freddy Callens<sup>\*,†</sup>

Department of Solid State Sciences, Ghent University, Krijgslaan 281-S1, B-9000 Gent, Belgium, Center for Molecular Modeling, Ghent University, Technologiepark 903, B-9052 Zwijnaarde, Belgium, and Department of Physics, University of Oslo, P.O. Box 1048 Blindern, N-0316 Oslo, Norway

Received: September 25, 2009; Revised Manuscript Received: November 4, 2009

Electron paramagnetic resonance (EPR), electron nuclear double resonance (ENDOR), and ENDOR-induced EPR (EIE) measurements on sucrose single crystals at 10 K after *in situ* X irradiation at this temperature reveal the presence of at least nine different radical species. Nine proton hyperfine coupling tensors were determined from ENDOR angular variations and assigned to six of these species (R1–R6) using EIE. Spectral simulations indicate that four of those (R1–R3 and R6) dominate the EPR absorption. Assisted by periodic density functional theory (DFT) calculations, R1 and R2 are identified as H-abstracted C1- and C5-centered radicals, R3 is tentatively assigned to an H-abstracted C6-centered radical, and R6 is identified as an alkoxy radical where the abstracted hydroxy proton has migrated to a neighboring OH group via intermolecular proton transfer. The latter radical had been characterized and identified in a previous study, but the present DFT calculations provide additional insight into its conformation and particular properties. This study provides the first step in unraveling the formation mechanism of the stable sucrose radicals detected after room-temperature irradiation and contributes to the understanding of the initial stages of radiation damage to solid-state carbohydrates.

## 1. Introduction

Direct radiation effects, i.e., processes initiated by radiation energy deposited at the target molecule itself and not its environment, in the deoxyribose moiety of DNA have been shown to lead to cleavage of sugar–phosphate bonds in the DNA backbone (single and double strand breaks). Such lesions may in turn result in cell death, cancer, and mutagenesis.<sup>1–3</sup> The complex structure of DNA necessitates the study of smaller model systems exhibiting key features similar to the deoxyribose-(–phosphate) moiety. In this context, carbohydrate single crystals are suitable model systems because the crystalline state to some extent mimics the rigid, tightly packed structure of chromosomal DNA, and similar general principles may be expected to govern the formation mechanisms of primary radicals in these systems. As carbohydrates are fundamental constituents of several biological systems, understanding their radiation physics and chemistry is also of a more general importance. A prerequisite to obtain such fundamental insight is, however, detailed knowledge of the electronic and molecular structure of the primary radiation-induced radicals.

In carbohydrate single crystals, X-ray irradiation mainly generates cations, i.e., one-electron-loss products, in the initial stage. The expelled electrons slow down through successive scattering events (producing secondary electrons) and are finally trapped either in a valence orbital of a molecule (yielding anions) or in a lattice void, between hydroxy groups of one or several neighboring molecules.<sup>4–12</sup> In general, the primary radicals then

undergo complex multistep processes of subsequent chemical reactions, eventually yielding either stable (usually neutral) radical species or diamagnetic products (recombination). Primary and intermediate radicals often are metastable, in which case they can be studied experimentally by irradiating the sample *in situ* at low temperatures and performing electron magnetic resonance (EMR) experiments without annealing.

As EMR experiments can provide a wealth of detailed structural information, such studies have been performed quite successfully for several carbohydrates and their derivatives (e.g., rhamnose,<sup>7a,8–10,12–14</sup> sucrose<sup>7a,11,15</sup> glucose-1-phosphate,<sup>16,17</sup> glucose,<sup>18,19</sup> methyl-glucose,<sup>20–23</sup>  $\beta$ -D-fructose,<sup>24,25</sup> and trehalose<sup>26,27</sup>). However, unambiguous identification of the major radical species based on EMR experimental data only remains very difficult, and often proves impossible. In recent years, highly accurate density functional theory (DFT) calculations on extended organic solid-state systems have become possible and practically available due to advances in computing power and density functionals, as well as to the development of new, more efficient codes for the calculation of EMR parameters.<sup>28,29</sup> Such calculations provide a powerful tool for the identification and detailed analysis of radical species. A combined approach extensively using different EMR methods and carefully designed DFT calculations has proven very successful for unambiguous identification and characterization of radiation-induced radicals as well as for the elucidation of their mechanisms of formation and decay.<sup>24,30–35</sup>

Sucrose (Figure 1) offers an extra advantage as a model system for DNA because the glycosidic bond bears similarity to the sugar–phosphate bond in the DNA backbone. Recently, we identified the chemical structures of the three major stable radiation-induced radicals in sucrose single crystals,<sup>34,36</sup> and the glycosidic bond was shown to be ruptured in all three. Detailed

\* To whom all correspondence should be addressed. Phone: 003292644352. Fax: 003292644996. E-mail: freddy.callens@ugent.be.

<sup>†</sup> Department of Solid State Sciences, Ghent University.

<sup>‡</sup> Center for Molecular Modeling, Ghent University.

<sup>§</sup> University of Oslo.

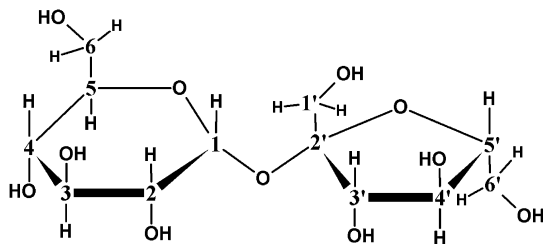


**Figure 1.** Chemical structure of the sucrose molecule with the atomic numbering used in the present work. Throughout this work, the following labeling scheme was used: HX and OX are the hydrogen and oxygen at CX, and HOX is the hydroxy proton at OX ( $X = 1-6, 1'-6'$ ).

knowledge of their formation mechanism is necessary to gain more fundamental insight into the associated radiation chemistry. As the stable radicals are formed in a short time span (minutes or less) upon room-temperature (RT) irradiation,<sup>37</sup> low-temperature, *in situ* X irradiation studies have to be employed and the current study is the first step toward this goal.

Low-temperature EMR studies on sucrose single crystals after *in situ* X irradiation at 4.2 K have been performed by others, revealing the presence of an alkoxy radical<sup>15</sup> and an intermolecularly trapped electron.<sup>7a,11</sup> In these studies, however, a large part of the electron paramagnetic resonance (EPR) absorption around  $g \approx 2.0030$  could not be attributed to either of those species and was not analyzed. In the present work, the results of EMR experiments on sucrose single crystals at 10 K after *in situ* X irradiation at this temperature are reported. Accompanying periodic DFT calculations have been performed with the goal of identifying the major radicals and gaining insight into their geometric and electronic structure.

## 2. Experimental and Computational Section

**2.1. Experimental Procedures.** Sucrose single crystals are monoclinic with space group  $P2_1$ , and a unit cell contains two molecules.<sup>38</sup> The  $\langle a^*bc \rangle$  system ( $\langle a^* \rangle$  being orthogonal to both  $\langle b \rangle$  and  $\langle c \rangle$ ) was chosen as the orthogonal reference frame, in analogy with our previous work.<sup>34,36,39</sup> The procedures for crystal growth have been described previously,<sup>39</sup> as well as those for sample orientation, preparation for EMR measurements and *in situ* X irradiation at 10 K (to doses of 45–60 kGy).<sup>40</sup> For the determination of the hyperfine coupling (HFC) tensors, EPR and electron nuclear double resonance (ENDOR) angular variation studies were made by rotating the crystals about the  $\langle a \rangle$ ,  $\langle b \rangle$ , and  $\langle c \rangle$  axes and about two other axes skewed with respect to the reference system (see Figure S1 in the Supporting Information) to eliminate ambiguities in the fitting results.<sup>41</sup> The program MAGRES<sup>42,43</sup> was used to derive the HFC tensors from the complete set of obtained ENDOR data, and Easyspin<sup>44</sup> routines were used for the simulation of the ENDOR angular variations.

**2.2. Computational Procedures.** All calculations were performed with the CP2K program package<sup>45</sup> in a periodic approach on an  $\langle ab2c \rangle$  supercell (i.e., the crystal unit cell doubled in the  $\langle c \rangle$  direction). Geometry optimizations were first done with the Gaussian and plane-waves (GPW) method,<sup>46</sup> with a plane-wave cutoff of 320 Ry (Ry), TZV2P GTH basis sets,<sup>47</sup> and GTH pseudopotentials.<sup>48,49</sup> Subsequently, geometries were further optimized in an all-electron approach using the Gaussian-augmented plane-wave (GAPW) method<sup>50</sup> with a plane-wave cutoff of 250 Ry and TZV2P basis sets. HFC-tensor<sup>28</sup> and  $g$ -tensor<sup>29</sup> calculations were also performed with the GAPW method at this level of theory. A BLYP functional<sup>51,52</sup> was

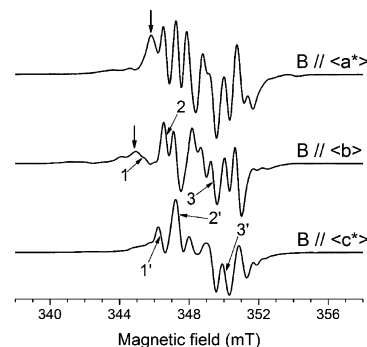


**Figure 2.** X-band EPR spectra of sucrose single crystals at 10 K after *in situ* X irradiation at 10 K for three different orientations of the crystal with respect to the magnetic field. All spectra are normalized to a microwave frequency of 9.7600 GHz. The numbered arrows indicate the positions at which the ENDOR spectra of Figure 4 were recorded. The vertical (not-numbered) arrows indicate absorption signals arising from the alkoxy radical that was reported and identified in ref 15 (labeled R6 in the current work).

employed for all calculations. The  $g$ -tensor calculations rely on a very recent implementation in CP2K.<sup>29</sup>

When calculated and experimental eigenvectors or crystal directions are compared, allowed symmetry operations ( $\langle b \rangle \rightarrow \langle -b \rangle$  and inversion of eigenvectors) are performed on the experimental eigenvectors to obtain the best possible agreement.

## 3. Results

**3.1. EPR, ENDOR, and EIE Spectra.** The EPR spectra obtained from sucrose single crystals at 10 K after *in situ* X irradiation at 10 K are shown in Figure 2 for three different orientations of the crystal in the external magnetic field. EPR angular variation studies in the three planes perpendicular to the principal crystallographic axes show that the bulk of the EPR absorption (between 346 and 353 mT in Figure 2) exhibits only small  $g$ -tensor anisotropy and is therefore likely due to carbon-centered radicals. For certain orientations, a broad absorption signal emerges at slightly lower field values. It will be shown in section 4.3 that this absorption can be attributed to the alkoxy radical previously reported by Box and Budzinski,<sup>15</sup> a species that has been labeled R6 in the present work. Other, more anisotropic EPR signals were observed, but these were very weak and were therefore not further investigated.

Extensive ENDOR measurements in the three planes perpendicular to the  $\langle a \rangle$ ,  $\langle b \rangle$ , and  $\langle c \rangle$  axes and in the two different skewed planes revealed a large number of proton HFC resonance lines. Enough data could be collected to determine the corresponding HFC tensors for nine HFC interactions and assign them to five different radical species R1–R5 (see below). These tensors are listed in Table 1. The Schonland ambiguity<sup>41</sup> was eliminated for all HFC tensors by including at least one of the skewed planes for their determination. The experimental ENDOR frequency positions and the simulations using the tensors of Table 1 are presented in Figure S1 of the Supporting Information. Measurements on deuterated sucrose single crystals indicate that all HFC interactions of Table 1 originate from nonexchangeable protons, except for HF1(R3), which therefore is due to a hydroxy proton. ENDOR and ENDOR-induced EPR (EIE) spectra reveal that there are at least three other radical species present, for which HFC tensors could not be determined. However, the EPR spectrum is dominated by contributions of only four radical species (R1, R2, R3, and R6), as will be shown in section 3.2.

**TABLE 1: Experimental Proton HFC Tensors (in MHz) for Radical Species R1–R6 in Sucrose Single Crystals, Determined from ENDOR Measurements at 10 K after *in situ* X Irradiation at This Temperature<sup>a</sup>**

radical	proton	iso	aniso	eigenvectors		
				<i>a</i> *	<i>b</i>	<i>c</i>
R1	HF1	100.61	−5.46	0.480	−0.591	−0.649
			−1.46	0.828	0.550	0.111
			6.92	0.292	−0.590	0.753
			−6.40	0.388	0.921	−0.019
R2	HF1	22.41	−3.53	0.829	−0.340	0.443
			9.93	0.402	−0.188	−0.896
			−5.93	0.759	−0.001	−0.651
			−4.80	0.272	0.909	0.316
R3	HF1	29.88	10.73	0.591	−0.417	0.690
			−11.05	0.568	0.777	−0.272
			−6.49	0.386	0.041	0.921
			17.54	0.727	−0.628	−0.277
R4	HF2	−54.21	−35.16	0.988	−0.095	−0.119
			0.12	0.042	0.923	−0.383
			35.05	0.146	0.373	0.916
			−12.52	0.308	0.794	0.524
R5	HF1	−48.08	0.93	0.028	−0.558	0.829
			11.60	0.951	−0.241	−0.194
			−30.75	0.098	−0.896	0.433
			4.71	0.973	−0.006	−0.232
R6	HF1	−50.56	26.04	0.211	0.444	0.871
			−1.90	0.176	−0.949	0.263
			−0.49	0.661	−0.084	−0.746
			2.39	0.730	0.305	0.612
R6	HF2	26.02	−10.70	0.708	−0.012	0.706
			−0.16	0.442	0.787	−0.430
			10.86	0.550	−0.617	−0.563

<sup>a</sup> The assignment to a total of six radical species was based on EIE measurements.

In Figure 3, two of the EPR spectra of Figure 2 are repeated, together with the corresponding EIE spectra of radicals R1–R6. Treating linewidths and *g* factors as variables, all EIE spectra could be accurately simulated using the HFC tensors listed in Table 1. R6 has a relatively large *g* anisotropy (compare parts a and b of Figure 3), and could be assigned to the alkoxy radical reported by Box and Budzinski;<sup>15</sup> the HF1(R6) and HF2(R6) HFC tensors (Table 1) indeed correspond well with tensors A1 and A3, respectively (as reported in ref 15 and reproduced in Table 2), with respect to both principal values (maximum deviation of about 0.5 MHz) and eigenvectors (maximum deviation of about 3°). We were unable to determine tensors for the other HFC interactions (A2, A4, A5, and A6 in Table 2), but clear evidence was found for their presence in the ENDOR and EIE spectra.

In a previous investigation, a trapped electron was observed at 4 K after *in situ* X irradiation at this temperature and was reported to be stable up to 61 K.<sup>7a,11</sup> However, the EPR, ENDOR, and EIE spectra obtained in our study do not yield any evidence for its presence at 10 K. Trapped electrons are known to decay upon exposure to UV or optical light, but the sample was kept in the dark during the irradiation and subsequent measurements. Another possibility would be that the proportion of the trapped electron dramatically decreases at high doses because it has a high destruction cross section. To investigate this, we have determined the dose dependency of the EPR spectrum in the dose range 3–45 kGy for six different orientations of the magnetic field. Although some minor differences are observed in relative line intensities between the EPR spectra recorded for different doses, the spectra agree well qualitatively and the presence of another radical species at lower

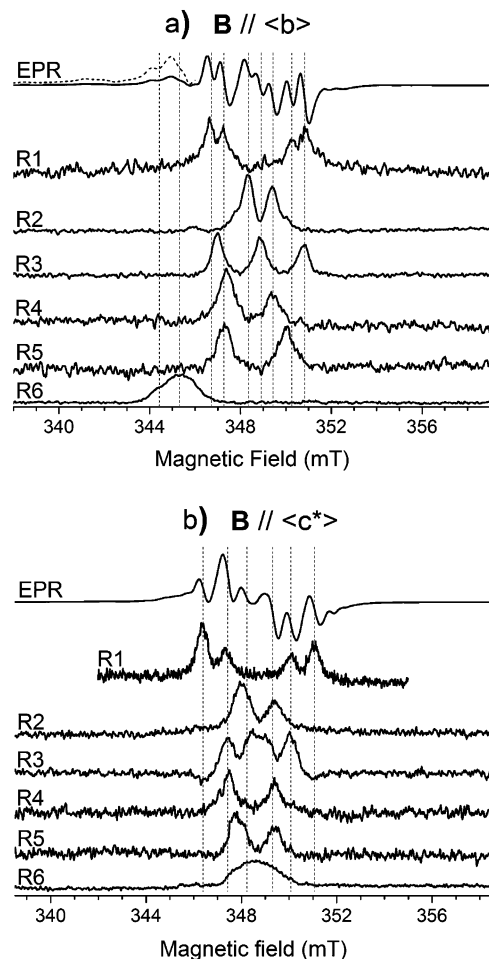


**Figure 3.** EPR spectrum and EIE spectra of radicals R1–R6 for (a)  $\mathbf{B} \parallel \langle \mathbf{b} \rangle$  and (b)  $\mathbf{B} \parallel \langle \mathbf{c}^* \rangle$ . All spectra are normalized to 9.7600 GHz. The dotted line in part a is the EPR spectrum multiplied by a factor of 3.

dose appears very unlikely. Therefore, the most plausible explanation for the absence of the trapped electron, in our opinion, is that the decay temperature reported in ref 7a is substantially overestimated (and is actually between 4 and 10 K). This is corroborated by the fact that, after *in situ* X irradiation at 3 K, UV bleaching (at 3 K) or annealing to 10 K yields EPR spectra very similar to those observed after *in situ* X irradiation at 10 K.<sup>7b</sup>

Figure 4 shows ENDOR spectra recorded at different magnetic field values for the two orientations in Figure 3. Each of the ENDOR lines associated with radical R1 is accompanied by one or several other lines, usually of weaker intensity. These lines were typically 0.2–0.5 MHz separated from the R1 ENDOR lines but exhibited the same ENDOR angular variation and yielded very similar EIE spectra. In Figure 4, these groups of HF1(R1) and “HF1(R1)-like” ENDOR lines are shown for both the high- and low-frequency branch (labeled A and B, respectively). Similar observations have been made for sorbose,<sup>53</sup> fructose,<sup>24</sup> and the stable radicals in sucrose,<sup>39</sup> and are most easily interpreted in terms of slightly different conformations of one radical species. This (resolved) spread of resonance lines decreases the ENDOR signal intensity, which would explain why the EIE spectra of R1 suffer from a relatively low signal-to-noise ratio (Figure 3), while on the other hand R1 accounts for a significant portion of the EPR spectrum (see section 3.2).



**TABLE 2: Experimental Proton HFC Tensors (in MHz) and  $g$  Tensor of an Alkoxy Radical Present in Sucrose Single Crystals at 4 K after *in situ* X Irradiation at This Temperature as Reported by Box and Budzinski<sup>15a</sup>**

HFC Tensors					
proton	iso	aniso	eigenvectors		
			$a^*$	$b$	$c$
A1	26.00	−1.82	0.205	0.942	0.262
		−0.54	0.644	0.071	−0.761
		2.36	0.736	−0.325	0.593
A2	15.09	−1.58	0.445	0.772	0.452
		−0.29	−0.246	−0.380	0.891
		1.87	0.860	−0.508	0.021
A3	10.05	−11.31	0.552	0.611	−0.566
		0.69	−0.407	0.791	0.456
		10.62	0.727	−0.021	0.686
A4	15.13	−5.59	0.926	−0.375	0.002
		−3.24	0.051	0.132	0.989
		8.83	0.372	0.917	−0.142
A5	−0.59	−5.09	0.417	0.752	0.510
		−4.47	0.129	−0.604	0.785
		9.57	0.899	−0.261	−0.349
A6	−1.11	−8.01	0.928	−0.356	0.100
		−6.59	−0.011	0.246	0.969
		14.61	0.370	0.901	−0.224

$g$ Tensor			
principal values	eigenvectors		
	$a^*$	$b$	$c$
2.0037	−0.072	−0.046	0.996
2.0087	0.889	−0.454	0.043
2.0270	0.450	0.889	0.074

<sup>a</sup> This species corresponds to radical R6 in the current study (Table 1).

When the samples are annealed to RT after *in situ* X irradiation at 10 K, the EPR spectra continuously transform (during annealing and at RT) and stabilize about 3 h after RT is reached. The final spectra correspond to those of the stable radicals obtained after RT irradiation.<sup>39</sup> Follow-up *in situ* X irradiation studies at elevated temperatures (80 and 140 K) and extensive thermal annealing studies, together with advanced DFT calculations, are currently being performed in our laboratories and will be the subject of a forthcoming publication.

**3.2. Relative Abundances of Different Radical Species.** As mentioned above, the EIE spectra of radicals R1–R6 recorded at the orientations  $\mathbf{B} \parallel \langle b \rangle$  and  $\mathbf{B} \parallel \langle c^* \rangle$  can be well reproduced using only the HFC tensors in Table 1. Taking the (isotropic)  $g$  values from the EIE simulations and treating the linewidths as variables, the experimental EPR spectra are already reproduced satisfactorily when only contributions of R1, R2, R3, and R6 are considered. The fit can be improved somewhat by mixing in small contributions of radicals R4 and R5. A relative contribution of 10% appears to be an upper limit for R4 as well as for R5, however, because larger concentrations give rise to features in the simulation that are not observed experimentally. By visual inspection, the following relative contributions were finally obtained as a best fit for the two orientations simultaneously (Figure 5): 15% R1, 20% R2, 30% R3, 5% R4, 5% R5, and 25% R6. The first-derivative spectra were normalized by setting the double integral to one.

The overall agreement between simulated and experimental spectra is good, even if there are some minor discrepancies with regard to relative line intensities. This indicates that all other

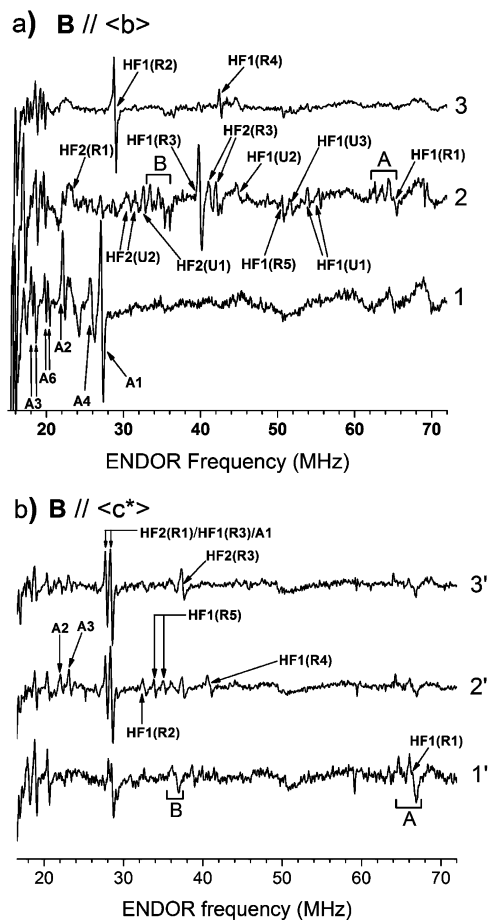


**Figure 4.** ENDOR spectra of sucrose single crystals at 10 K after *in situ* X irradiation at 10 K for (a)  $\mathbf{B} \parallel \langle b \rangle$  and (b)  $\mathbf{B} \parallel \langle c^* \rangle$ . The numbers on the right-hand side indicate at which positions in the EPR spectra (cf. Figure 2) the ENDOR spectra were recorded. Proton ENDOR lines are labeled according to the labeling scheme of Table 1. For R6, however, the labeling scheme of Table 2 is used: A1–A6, where A1 = HF1(R6) and A3 = HF2(R6). Additional lines, for which HFC tensors could not be determined, are labeled HF1(U1), HF2(U1), HF1(U2), HF2(U2), and HF1(U3). These lines have been associated by EIE with three different radicals U1–U3. The letters “A” and “B” indicate high- and low-frequency ENDOR lines, respectively, originating from radical species R1 and “R1-like” (see text).

radicals indeed are minority species. This study therefore provides further evidence that radiation damage occurs selectively, as is generally assumed.

## 4. Discussion

**4.1. DFT-Assisted Identification of R1 and R2.** Radical R1 exhibits two typical  $\beta$ -proton HFCs (Table 1). Using the point-dipole approximation, carbon atom C5 emerges as the most plausible radical center: the eigenvectors associated with the most positive principal values ( $V_{+2b}$ ) of HFC tensors HF1(R1) and HF2(R1) make angles of approximately 17 and 3° with the  $C5 \cdots H4$  and  $C5 \cdots H6b$  directions, respectively, in the pristine lattice. Assuming net H-abstraction, one arrives at model M1 (Figure 6). The DFT-calculated HFC tensors for M1 agree well with the experimentally obtained tensors in all aspects (Table 3), providing convincing evidence that M1 is the chemical structure of radical species R1.

Radical R2 is characterized by only one significant  $\beta$ -proton HFC, and the point-dipole approximation here yields C1, C4, and C5 as the most plausible sites for the unpaired electron: angles of 3–4° are calculated between the  $V_{+2b}$  eigenvector of

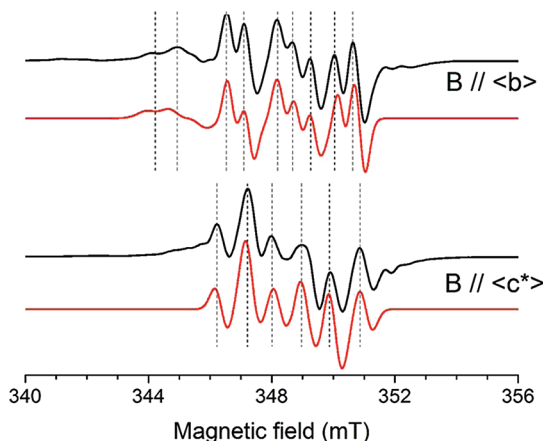


**Figure 5.** Experimental (black) and simulated (red) EPR spectra for two different orientations of the crystal in the magnetic field (cf. Figure 2). The simulations include contributions of radical species R1–R6, with the relative concentrations as given in the text (section 3.2). See text for further details.

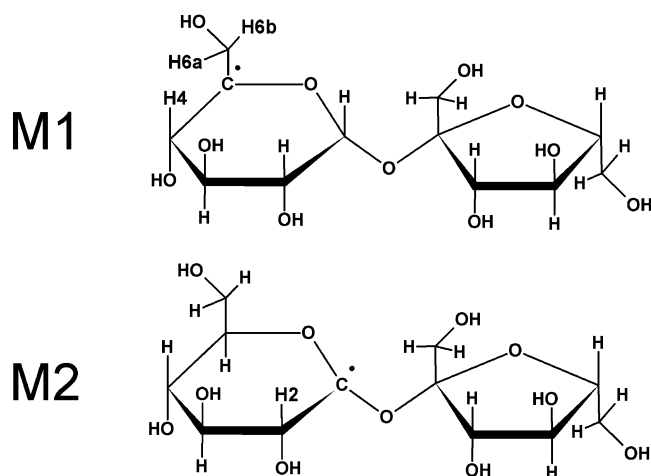


**Figure 6.** Chemical structure of radical models M1 and M2 for radical species R1 and R2, respectively. The DFT-calculated proton HFC tensors are given in Table 3.

**TABLE 3: DFT-Calculated Proton HFC Tensors (in MHz) for Radical Models M1 and M2 (Figure 6)<sup>a</sup>**

radical model	proton	iso	aniso	eigenvectors			$\delta$ (deg)
				$a^*$	$b$	$c$	
M1	H4	91.61	-5.68	0.375	-0.604	-0.703	HF1(R1)
			-1.08	0.846	0.533	-0.007	7
			6.75	0.379	-0.592	0.711	6
	H5	15.84	-5.79	0.201	0.971	-0.128	HF2(R1)
			-3.49	0.894	-0.128	0.429	13
			9.28	0.400	-0.201	-0.894	1
M2	H2	28.88	-6.01	0.733	-0.082	-0.675	HF1(R2)
			-4.41	0.370	0.881	0.295	5
			10.42	0.571	-0.466	0.676	6
							3

<sup>a</sup>  $\delta$  is the angle between the computed and corresponding experimental eigenvectors (Table 1).

HF1(R2) and C1...H2, C4...H5, and C5...H4, respectively. Again, only considering net H-abstraction events, DFT calculations yield a good agreement with experimental data only for the C1-centered species (M2 in Figure 6). The calculated tensors for M2 and the C5-centered species (M1, see above) are given in Table 3, and those for the C4-centered species, in the Supporting Information (Table S1).

We also note that the DFT calculations do not predict any other proton HFC interaction that should have been detected

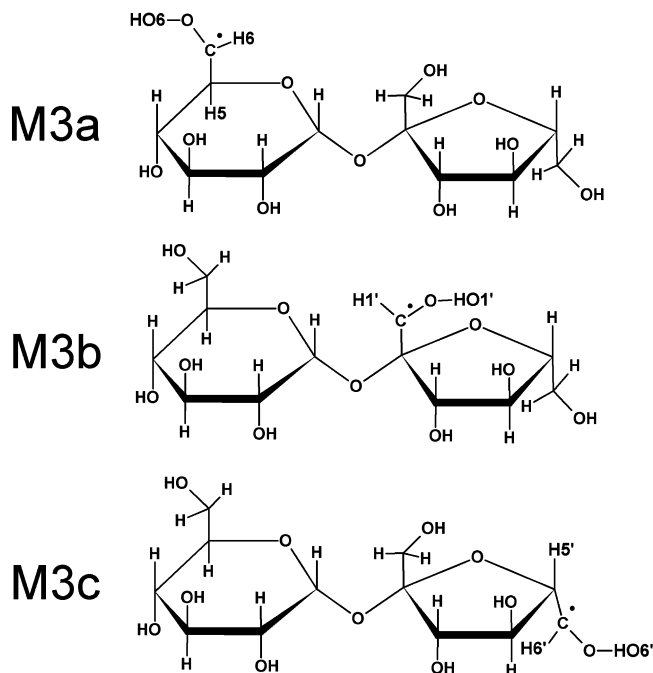


**Figure 7.** Chemical structure of radical models M3a–M3c proposed for radical species R3. The DFT-calculated proton HFC tensors are given in Table 4.

experimentally, which further strengthens these radical model assignments.

#### 4.2. Tentative DFT-Assisted Identification of Radical R3.

For radical R3, two significant proton HFC interactions are detected (Table 1). The HF1(R3) coupling is due to a hydroxy proton (section 3.1), and the magnitude of the isotropic and anisotropic components indicates that it is in a  $\beta$  position.<sup>54</sup> The HF2(R3) tensor is typical for a HFC interaction with an  $\alpha$ -proton. Judging by the maximum positive dipolar coupling and the relative values of this component and the isotropic HFC value, the spin density at  $C_\alpha$  is  $\sim 0.90$  and the center possibly is slightly bent.<sup>55</sup> If only net H-abstraction events are considered, there are three possible radical sites: C6, C1', and C6'. The corresponding models are depicted in Figure 7 and labeled M3a, M3b, and M3c, respectively.

The  $\bar{V}_{+a}$  eigenvector of an  $\alpha$ -proton HFC with anisotropic values  $\sim(-a, 0, +a)$  is roughly parallel to the  $C_\alpha-H_\alpha$  bond, while the  $\bar{V}_0$  eigenvector is roughly parallel to the lone-electron orbital (LEO) axis. Assuming a planar  $C-C_\alpha H_\alpha OH$  fragment ( $sp^2$  hybridization),  $C_\alpha-H_\alpha$  should lie approximately along the bisector of the angle formed by C,  $C_\alpha$ , and O and the LEO axis should be perpendicular to the plane formed by those atoms. Under these assumptions and using the atomic coordinates of the pristine lattice, the angle between  $C_\alpha-H_\alpha$  and  $\bar{V}_{+a}$  is 9, 47, and 51° and the angle between  $\bar{V}_0$  and the LEO is 24, 62, and 70° for models M3a, M3b, and M3c, respectively. These numbers suggest M3a as the most plausible model. M3a also gives the best results when the  $C-C_\alpha H_\alpha OH$  fragment is assumed to retain the  $sp^3$ -hybridized structure of the intact fragment: an angle of 18° between  $\bar{V}_{+a}$  and  $C_\alpha-H_\alpha$  is found, and an angle of 2° between  $\bar{V}_0$  and the LEO (which lies along the broken C–H bond in this case).

The hydroxymethyl group may have considerable conformational freedom, however, and DFT calculations were performed for all three models. The calculated HFC tensors are given in Table 4. Unfortunately, none of the models yield a convincing agreement with the experimental data. M3a perhaps yields the best results, but the discrepancies still are considerable.

**TABLE 4: DFT-Calculated Proton HFC Tensors (in MHz) for Radical Models M3a–M3c (Figure 7)<sup>a</sup>**

model	proton	iso	aniso	eigenvectors			$\delta$ (deg)
				$a^*$	$b$	$c$	
M3a	H6	−50.23	−34.69	0.980	0.067	−0.188	HF2(R3) 10
			−2.68	−0.180	0.697	−0.694	26
			37.36	0.085	0.714	0.695	24
	HO6	75.79	−12.96	0.259	−0.082	−0.962	HF1(R3) 70
			−8.76	0.794	0.585	0.164	61
			21.72	0.550	−0.807	0.217	32
M3b	H5	15.18	−6.73	0.260	−0.497	0.828	
			−4.05	0.113	0.867	0.485	
			10.78	0.959	0.032	−0.281	
	H1'	−44.45	−33.58	0.352	0.237	−0.905	HF2(R3) 64
			−3.02	0.872	0.269	0.410	83
			36.61	−0.341	0.934	0.111	66
M3c	HO1'	25.05	−12.44	0.578	0.257	0.774	HF1(R3) 71
			−9.63	−0.766	−0.154	0.624	74
			22.07	0.279	−0.954	0.108	39
	H6'	−53.68	−33.60	0.603	0.727	−0.327	HF2(R3) 55
			−1.86	−0.779	0.450	−0.437	57
			35.47	−0.171	0.518	0.838	21
	HO6'	17.62	−10.36	0.916	−0.282	0.284	HF1(R3) 77
			−9.32	−0.400	−0.651	0.645	66
			19.68	0.003	−0.705	−0.709	50
	H5'	1.68	−6.19	−0.081	0.577	0.813	
			−4.32	0.765	−0.486	0.422	
			10.51	0.639	0.656	−0.402	

<sup>a</sup>  $\delta$  is the angle between the computed and corresponding experimental eigenvectors (Table 1).

A possible explanation is the existence of another (local) minimum on the potential energy surface (PES) that does correspond to the experimentally observed radical geometry. The most obvious degree of freedom in a C–C<sub>α</sub>H<sub>α</sub>OH fragment is the rotation of the OH group about the C<sub>α</sub>–O bond axis. Energy profiles were constructed for these rotations in models M3a, M3b, and M3c by performing geometry optimizations with the C–C<sub>α</sub>–O–H dihedral angle constrained to values between 0 and 345° in 15° steps (the same methodology as applied in, e.g., ref 34). Several alternative local minima were found, but none yield HFC tensors that agree better with the experimental data. For M3a, the most plausible model, similar scans for the hydroxy groups of neighboring molecules that are hydrogen bound to O6 or HO6 did also not yield any relevant result.

Approaching the problem differently, we investigated whether the geometry of the C–C<sub>α</sub>H<sub>α</sub>OH fragments for any of the three models (M3a–M3c) can be altered in a plausible way such that the calculated tensors are in better agreement with experimental data. It appears that this can only be achieved for M3a: starting from the DFT-optimized geometry, limited (<15°) reorientation of the C<sub>α</sub>H<sub>α</sub> bond so that the radical center is more planar and a rotation of the O6–HO6 hydroxy group about the C6–O6 bond axis with about 25° suffices to give a rather good agreement for both HFC tensors (see Table S2 in the Supporting Information). The calculations still predict a small HFC interaction with the H5 proton, but this may well escape detection both in ENDOR (due to the multitude of ENDOR lines in that region, especially those associated with R6) and in EIE (a coupling of that size would only cause broadening of the resonance lines). The fact remains, however, that this conformation does not correspond to a local minimum on the PES. As the current computational methodology has proven successful for several other, similar radical structures,<sup>34–36</sup> the most plausible explanation, in our opinion, is the presence of a (diamagnetic) fragment as a side product of the radical formation: this could alter the PES such that the conformation mentioned above does correspond to a local minimum. In section

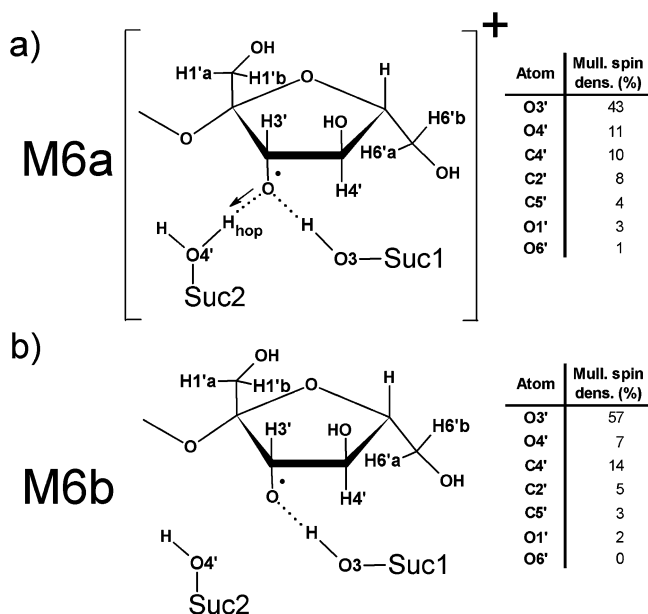


**Figure 8.** Chemical structure of radical models M6a and M6b for radical species R6. M6a is a single positively charged species where the abstracted HO3' proton has migrated to the hydrogen-bound O4' oxygen of a neighboring molecule (Suc2). M6b is neutral, as the HO3' hydrogen is removed altogether. The DFT-calculated proton HFC tensors for M6a are given in Table 5, and those for M6b, in Table S2 of the Supporting Information. DFT-calculated  $g$  tensors are given in Table 6. At the right-hand side, the Mulliken spin densities (Mull. spin dens.) as reported by CP2K are presented for some selected atoms.

4.5, a possible mechanism will be presented which results in the formation of an H<sub>2</sub> molecule (which may be expected to have very limited mobility at 10 K) near the radical center. Testing this hypothesis is not a trivial task and falls outside the scope of the current study.

In conclusion, the available evidence points toward (some conformation of) the M3a model but other radical models cannot be excluded with certainty at present. However, based on the calculations, M3b and M3c do not appear very plausible and other radical species of the structure R–C'HOH require considerable structural reorganization (such as ring-opening events) of the pristine molecule, which seem less likely at 10 K.

**4.3. Radical Species R6.** As noted in section 3.1, this is the alkoxy radical thoroughly characterized by Box and Budzinski.<sup>15</sup> The six proton HFC tensors reported in that work (Table 2) will be used here, since only two HFC tensors could be determined in the current study (Table 1). Box and Budzinski assigned the HFC interactions to structure M6a depicted in Figure 8a: an O3'-centered alkoxy radical where the HO3' proton (labeled H<sub>hop</sub>) has migrated to the O4' oxygen of a neighboring molecule (Suc2 in Figure 8a), to which it is hydrogen-bound in the pristine lattice. The DFT geometry optimization yields a stable conformation where the local hydrogen-bonding network is rearranged (Conf1 in Figure 9b). The HFC and  $g$  tensors calculated for Conf1 of M6a are given in Tables 5 and 6, respectively. All HFC tensors with substantial principal values have been reported in Table 5. The overall agreement between experimental and calculated HFC and  $g$  tensors is striking and confirms the model assignment by Box and Budzinski. In particular, a strongly reduced  $g$  anisotropy is indeed predicted. The attribution of the HFC interactions to the different protons by Box and Budzinski is correct for A3–A6 (although the DFT calculations indicate the sign of the A3 tensor should be

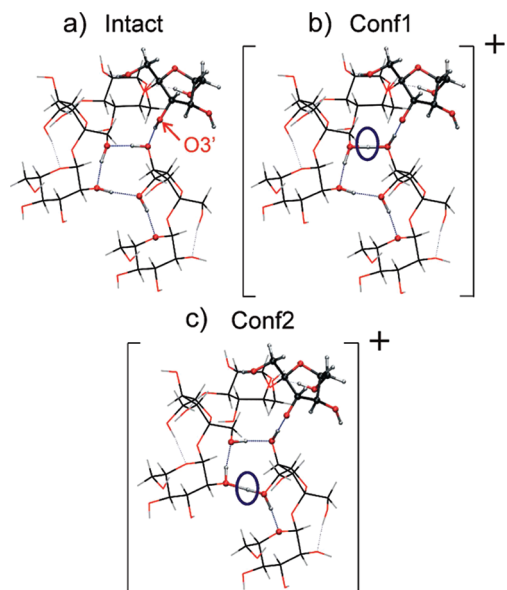


**Figure 9.** Periodically optimized geometries of (a) the intact lattice and conformations (b) Conf1 and (c) Conf2 of radical model M6a (Figure 8a). The O3' hydrogen is part of a hydrogen-bonding network (blue dotted lines) terminating in the ring oxygen of the glucose unit of a neighboring molecule. Conf1 and Conf2 have a net positive charge. The DFT-calculated proton HFC tensors of Conf1 are given in Table 5, and those of Conf2, in Table S3 of the Supporting Information. The circles in parts b and c indicate where the transferred proton is located.

**TABLE 5: DFT-Calculated Proton HFC Tensors (in MHz) for Conformation Conf1 (Figure 9b) of Radical Model M6a (Figure 8a)<sup>a</sup>**

proton	iso	aniso	eigenvectors			$\delta$ (deg)
			$a^*$	$b$	$c$	
H1'b	41.70	-2.10	0.165	0.941	0.296	A1 4
			-0.60	0.497	-0.849	12
			2.70	0.852	-0.287	11
H6'a	19.35	-1.47	0.362	0.750	0.554	A2 8
			-0.30	-0.319	-0.459	7
			1.76	0.876	-0.477	4
H4'	-5.75	-6.80	0.710	0.025	0.703	A3 3
			-1.03	-0.421	0.815	4
			7.83	0.564	0.578	3
H3'	-4.02	-4.47	0.902	-0.359	0.240	A4 14
			-3.12	-0.138	0.287	14
			7.59	0.409	0.888	5
HO3(Suc1)	-0.59	-4.79	0.377	0.815	0.209	A5 6
			-4.33	0.230	-0.543	7
			9.12	0.897	-0.203	5
H <sub>hop</sub>	-1.48	-7.09	0.921	-0.385	-0.066	A6 10
			-6.14	0.154	0.203	10
			13.24	0.358	0.900	2
HO4'	-1.63	-7.56	-0.860	-0.469	-0.201	
			-3.38	-0.502	0.711	
			10.94	0.088	-0.525	
H5'(Suc1)	9.26	-3.72	-0.905	-0.187	0.383	
			-1.98	0.123	0.745	
			5.70	0.408	-0.640	

<sup>a</sup>  $\delta$  is the angle between the computed and corresponding experimental eigenvectors (Table 2).

reversed) but not for A1 and A2: the calculations show that these originate from H1'b and H6'a, a  $\delta$  and an  $\epsilon$  proton, respectively, and not from protons H1'a and H1'b, as suggested by Box and Budzinski.<sup>15</sup> Substantial isotropic couplings to remote protons have been reported before for alkoxy radicals:

**TABLE 6: DFT-Calculated  $g$  Tensors for Conformations Conf1 and Conf2 (Figure 9b and c, Respectively) of Radical Model M6a (Figure 8a) and for Radical Model M6b (Figure 8b)<sup>a</sup>**

		princ	eigenvectors			$\delta$ (deg)
			$a^*$	$b$	$c$	
M6a	Conf1	2.0057	-0.011	0.022	1.000	4
		2.0102	-0.928	-0.373	-0.002	6
		2.0210	0.373	-0.927	0.024	6
	Conf2	2.0055	-0.019	0.011	1.000	4
		2.0098	-0.886	-0.464	-0.012	3
		2.0211	0.464	-0.886	0.019	4
M6b		2.0044	-0.288	-0.177	0.941	18
		2.0091	-0.702	-0.630	-0.333	22
		2.0324	0.652	-0.756	0.057	14

<sup>a</sup>  $\delta$  is the angle between the computed and corresponding experimental eigenvectors (Table 2).

in rhamnose, a  $\delta$  proton with an isotropic HFC value of 76 MHz was even observed.<sup>14</sup>

In spite of the generally good agreement, some discrepancies are encountered between calculated and experimental isotropic HFC values, e.g., for H3' (-4 MHz in the DFT calculation (Table 5) versus 15 MHz experimentally (A4, Table 2)). Also, an isotropic value of about 9 MHz is calculated for the H5'(Suc1) tensor (Table 5), which was not reported experimentally.<sup>15</sup> Since isotropic HFC values are known to be more sensitive to the level of theory and the positive charge of the structure may render periodic calculations less accurate,<sup>35</sup> these discrepancies do not invalidate model M6a.

The alkoxy radical under study has two peculiar properties: a relatively small  $g$  anisotropy and a high degree of spin polarization (reflected in the isotropic HFC value) at particular, remote protons (Table 2). To assess the possible role of the transferred HO3' proton (H<sub>hop</sub> in Figure 8a), DFT calculations were performed on model M6b (Figure 8b), where it is removed. In spite of some considerable differences between the HFC tensors calculated for Conf1 of M6a (Table 5) and M6b (Table S3 of the Supporting Information), especially with regard to isotropic values, which are actually better reproduced in M6b, the results are qualitatively comparable. Similarly, although the  $g$ -tensor anisotropy is considerably larger for M6b than for Conf1 of M6a, it still is (very) small for an alkoxy radical (Table 6). Thus, although the transferred proton noticeably influences the EMR properties of the radical, its presence apparently is not crucial for the aforementioned properties.

As noted above, the A6 HFC tensor (Table 2) can be readily attributed to the transferred proton. This raises the question whether further proton transfer events occur and, if so, where the chain of proton transfers finally terminates. A previous study on rhamnose suggests that successive proton transfers along hydrogen bonds may occur until the proton is trapped in a lattice defect or recombines with a (radical) anion.<sup>56</sup> In the present case, the hydrogen bonding network in the pristine lattice terminates at the ring oxygen of a glucose unit, five hydrogen bonds away from O3' (Figure 9a). Conformations resulting from subsequent proton transfer events along this hydrogen bond chain were considered. Apart from Conf1 (Figure 9b), one other conformation was found that apparently corresponds to a local minimum on the PES: Conf2 (4 proton "hops"), depicted in Figure 9c. Other initial conformations were found to be unstable and readily transformed to either Conf1 or Conf2. The calculated HFC tensors and  $g$  tensor of Conf2 (Table S4 of the Supporting Information and Table 6, respectively) are quite similar to those



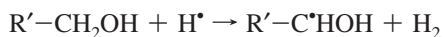
of Conf1 (although the agreement with experimental data is somewhat better for Conf1), so that we should rely on energy considerations. Since Conf2 is 14 kJ/mol higher in energy than Conf1, extended proton transfer events appear unlikely for the present alkoxy radical.

**4.4. Radical Species R4 and R5.** Suitable H-abstracted radical models cannot readily be found for R4 and R5. As discussed in section 3.2, these are minor species and therefore no further (thorough) attempts were made to identify them. Some brief comments will be made here.

The EIE spectra of radical species R4 (Figure 3) are broad-line doublets. Only for the major HFC interaction a HFC tensor could be extracted (HF1(R4) in Table 1). The magnitude of the principal values may indicate that the proton is in the proximity of the radical center, but the anisotropy is too small for an  $\alpha$  proton and has a symmetry atypical for a  $\beta$  proton. The anisotropic HFC values do, however, resemble those of certain  $\gamma$  protons in alkoxy radicals (e.g., A3 in Table 2). On the other hand, the EIE spectra of Figure 3 indicate that R4 has principal  $g$  values slightly larger than those of common carbon-centered radicals but still considerably smaller than those of alkoxy radicals. Limited (<20%) delocalization of the spin density onto an oxygen may explain both this and the HF1(R4) tensor. Also note that the principal values of HF1(R4) may have signs opposite to those in Table 1.

Radical species R5 is also characterized by a broad-line doublet, and again, only the HFC tensor of the major HFC interaction could be determined (HF1(R5) in Table 1). It has the typical characteristics of an  $\alpha$ -proton. As discussed in section 4.2, only three simple H-abstracted radical models may be envisaged initially: M3a, M3b, and M3c in Figure 7 (DFT-calculated tensors in Table 4). Model M3c (C6'-centered) yields the best agreement with regard to the eigenvector directions of the  $\alpha$ -proton HFC, but the deviations appear to be too large: 22, 49, and 43°. Also, the EIE spectra do not accommodate the DFT-calculated HFC tensor of HO6'.

**4.5. Oxidation and Reduction Products.** The trapped electron detected at 4 K is located near the C5–C6 and C6–O6 bonds<sup>7a,11</sup> and has been observed to decay upon light bleaching or thermal annealing into one or more carbon-centered radicals.<sup>7b</sup> Both R1, which is C5-centered (section 4.1), and R3, supposedly C6-centered (section 4.2), may therefore be *reduction* products resulting (indirectly) from electron capture. One possible reaction sequence for a C6-centered radical species is<sup>27</sup>



An  $\text{H}_2$  molecule is then formed and possibly trapped near the radical center, which may explain why we were not able to find a stable conformation of radical model M3a that yields good agreement with experimental HFC tensors (section 4.2). An analogous formation mechanism is of course possible for a C5-centered species.

As the abstracted proton is still present in radical R6, this very likely is an *oxidation* product. Using the values given in section 3.2, R1 and R3 (assumedly reduction products) account for 45% of the EPR absorption and R6 (oxidation product) for 25%. In order to achieve a balance, R2 (20%) should then be an oxidation product. This reasoning is of course very speculative at present.

## 5. Conclusion

Upon X irradiation at 10 K, four major radical species (R1–R3 and R6) are formed in sucrose single crystals. Three

of them (R1–R3) are carbon-centered: R1 and R2 are obtained by H abstraction from carbon atoms C5 and C1, respectively, and R3 has tentatively been assigned to an H-abstracted, C6-centered radical. R6 is an alkoxy radical where proton transfer has taken place along a hydrogen bond to an oxygen atom on a neighboring molecule. The identification of these species provides the necessary first step in both mapping the initial stages of radiation damage in a solid-state carbohydrate and unraveling the formation mechanisms of the major stable sucrose radicals, which involve glycosidic bond scission and carbonyl group formation.

**Acknowledgment.** This work was financially supported by the COST (European Cooperation in the field of Scientific and Technical Research), action P15. The authors acknowledge a Postdoctoral Fellowship (E.P. and H.V.) and a Research Assistant Fellowship (H.D.C.) with the Flemish Research Foundation (FWO-Vlaanderen). Part of the computational resources and services used in this work were provided by Ghent University.

**Supporting Information Available:** Tables showing DFT-calculated proton HFC tensors for the H-abstracted C4-centered radical, for model M6a in a conformation obtained by a geometry optimization with constraints on the coordinates of C5, C6, O6, and HO6, for model M6b, and for conformation Conf2 of model M6a and figure showing angular variation of the ENDOR transitions in sucrose single crystals, measured at 10 K after *in situ* X irradiation at this temperature, for the HFC interactions associated with radicals R1–R6 in the three planes perpendicular to the direct crystal axes, and in two different skewed planes. This material is available free of charge via the Internet at <http://pubs.acs.org>.

## References and Notes

- (1) Pogozelski, W. K.; Tullius, T. D. *Chem. Rev.* **1998**, 98, 1089–1107.
- (2) Bernhard, W. A.; Close, D. M. DNA Damage Dictates the Biological Consequences of Ionizing Irradiation: The Chemical Pathways. In *Charged Particle and Photon Interactions with Matter: Chemical, Physicochemical, and Biological Consequences with Applications*; Mozumder, A., Hatano, Y., Eds.; Marcel Dekker: New York, 2003; Vol. 43, pp 1–470.
- (3) Becker, D.; Adhikary, A.; Sevilla, M. D. The Role of Charge and Spin Migration in DNA Radiation Damage. In *Charge Migration in DNA Physics, Chemistry and Biology Perspectives*; Chakraborty, T., Ed.; Springer-Verlag: Berlin, Heidelberg, 2007; Vol. 13, pp 9–175.
- (4) Box, H. C. *Radiation Effects: ESR and ENDOR analysis*; Academic Press, Inc.: New York, 1977.
- (5) Box, H. C.; Budzinski, E. E.; Freund, H. G. *J. Chem. Phys.* **1978**, 69, 1309.
- (6) Box, H. C.; Budzinski, E. E.; Freund, H. G.; Potter, W. R. *J. Chem. Phys.* **1979**, 70, 1320.
- (7) (a) Budzinski, E. E.; Potter, W. R.; Potienko, G.; Box, H. C. *J. Chem. Phys.* **1979**, 70, 5040–5044. (b) Samskog, P.-O.; Kispert, L. D.; Lund, A. Sagstuen, E. Personal communication, 1985.
- (8) Samskog, P. O.; Lund, A.; Nilsson, G.; Symons, M. C. R. *J. Chem. Phys.* **1980**, 73, 4862–4866.
- (9) Samskog, P. O.; Kispert, L. D.; Lund, A. *J. Chem. Phys.* **1983**, 79, 635–638.
- (10) Box, H. C.; Budzinski, E. E.; Freund, H. G. *Radiat. Res.* **1990**, 121, 262–266.
- (11) Box, H. C.; Budzinski, E. E.; Freund, H. G. *J. Chem. Phys.* **1990**, 93, 262–266.
- (12) Sagstuen, E.; Lindgren, M.; Lund, A. *Radiat. Res.* **1991**, 128, 235–242.
- (13) Samskog, P. O.; Lund, A. *Chem. Phys. Lett.* **1980**, 75, 525–527.
- (14) Budzinski, E. E.; Box, H. C. *J. Chem. Phys.* **1985**, 82, 3487–3490.
- (15) Box, H. C.; Budzinski, E. E. *J. Chem. Phys.* **1983**, 79, 4142–4145.
- (16) Locher, S. E.; Box, H. C. *J. Chem. Phys.* **1980**, 72, 828–832.
- (17) De Cooman, H.; Vanhaelewyn, G.; Pauwels, E.; Sagstuen, E.; Waroquier, M.; Callens, F. *J. Phys. Chem. B* **2008**, 112, 15045–15053.

- (18) Madden, K. P.; Bernhard, W. A. *J. Phys. Chem.* **1979**, *83*, 2643–2649.
- (19) Madden, K. P.; Bernhard, W. A. *J. Phys. Chem.* **1982**, *86*, 4033–4036.
- (20) Madden, K. P.; Bernhard, W. A. *Radiat. Res.* **1978**, *74*, 486.
- (21) Madden, K. P.; Bernhard, W. A. *J. Chem. Phys.* **1979**, *70*, 2431–2437.
- (22) Madden, K. P.; Bernhard, W. A. *J. Phys. Chem.* **1980**, *84*, 1712–1717.
- (23) Madden, K. P.; Bernhard, W. A. *J. Chem. Phys.* **1980**, *72*, 31–33.
- (24) Vanhaelewyn, G.; Pauwels, E.; Callens, F.; Waroquier, M.; Sagstuen, E.; Matthys, P. *J. Phys. Chem. A* **2006**, *110*, 2147–2156.
- (25) Tarpan, M. A.; Sagstuen, E.; Pauwels, E.; Vrielinck, H.; Waroquier, M.; Callens, F. *J. Phys. Chem. A* **2008**, *112*, 3898–3905.
- (26) Samskog, P.-O.; Kispert, L. D.; Lund, A. *J. Chem. Phys.* **1982**, *77*, 2330–2335.
- (27) Samskog, P.-O.; Kispert, L. D.; Lund, A. *J. Chem. Phys.* **1983**, *78*, 5790–5794.
- (28) Declerck, R.; Pauwels, E.; Van Speybroeck, V.; Waroquier, M. *Phys. Rev. B* **2006**, *74*, 245103.
- (29) Weber, V.; Iannuzzi, M.; Giani, S.; Hutter, J.; Declerck, R.; Waroquier, M. *J. Chem. Phys.* **2009**, *131*, 014106.
- (30) Øhman, K. T.; Sanderud, A.; Hole, E. O.; Sagstuen, E. *J. Phys. Chem. A* **2006**, *110*, 9585–9596.
- (31) Pauwels, E.; Van Speybroeck, V.; Waroquier, M. *J. Phys. Chem. A* **2006**, *110*, 6504–6513.
- (32) Jayatilaka, N.; Nelson, W. H. *J. Phys. Chem. B* **2007**, *111*, 800–810.
- (33) Jayatilaka, N.; Nelson, W. H. *J. Phys. Chem. B* **2007**, *111*, 7887–7896.
- (34) De Cooman, H.; Pauwels, E.; Vrielinck, H.; Sagstuen, E.; Callens, F.; Waroquier, M. *J. Phys. Chem. B* **2008**, *112*, 7298–7307.
- (35) Pauwels, E.; De Cooman, H.; Vanhaelewyn, G.; Sagstuen, E.; Callens, F.; Waroquier, M. *J. Phys. Chem. B* **2008**, *112*, 15054–15063.
- (36) De Cooman, H.; Pauwels, E.; Vrielinck, H.; Sagstuen, E.; Van Doorslaer, S.; Callens, F.; Waroquier, M. *Phys. Chem. Chem. Phys.* **2009**, *11*, 1105–1114.
- (37) Vrielinck, H.; De Cooman, H.; Karakirova, Y.; Yordanov, N. D.; Callens, F. *Radiat. Res.* **2009**, *172*, 226–233.
- (38) Brown, G. M.; Levy, H. A. *Acta Crystallogr., Sect. B* **1973**, *29*, 790–797.
- (39) De Cooman, H.; Pauwels, E.; Vrielinck, H.; Dimitrova, A.; Yordanov, N. D.; Sagstuen, E.; Waroquier, M.; Callens, F. *Spectrochim. Acta, Part A* **2008**, *69*, 1372–1383.
- (40) Tarpan, M. A.; Sagstuen, E.; Pauwels, E.; Vrielinck, H.; Waroquier, M.; Callens, F. *J. Phys. Chem. A* **2008**, *112*, 3898–3905.
- (41) Vrielinck, H.; De Cooman, H.; Tarpan, M. A.; Sagstuen, E.; Waroquier, M.; Callens, F. *J. Magn. Reson.* **2008**, *195*, 196–205.
- (42) Nelson, W. H. *J. Magn. Reson.* **1980**, *38*, 71–78.
- (43) Sørnes, A. R.; Sagstuen, E.; Lund, A. *J. Phys. Chem.* **1995**, *99*, 16867–16876.
- (44) Stoll, S.; Schweiger, A. *J. Magn. Reson.* **2006**, *178*, 42.
- (45) <http://cp2k.berlios.de>.
- (46) Lippert, G.; Hutter, J.; Parrinello, M. *Mol. Phys.* **1997**, *92*, 477.
- (47) Lippert, G.; Hutter, J.; Ballone, P.; Parrinello, M. *J. Phys. Chem.* **1996**, *100*, 6231–6235.
- (48) Goedecker, S.; Teter, M.; Hutter, J. *Phys. Rev. B* **1996**, *54*, 1703–1710.
- (49) Hartwigsen, C.; Goedecker, S.; Hutter, J. *Phys. Rev. B* **1998**, *58*, 3641–3662.
- (50) Lippert, G.; Hutter, J.; Parrinello, M. *Theor. Chem. Acc.* **1999**, *103*, 124.
- (51) Becke, A. D. *Phys. Rev. A* **1988**, *38*, 3098–3100.
- (52) Lee, C.; Yang, W.; Parr, R. G. *Phys. Rev. A* **1988**, *37*, 785.
- (53) Vanhaelewyn, G.; Jansen, B.; Pauwels, E.; Sagstuen, E.; Waroquier, M.; Callens, F. *J. Phys. Chem. A* **2004**, *108*, 3308–3314.
- (54) Ko, C.-L.; Box, H. C. *J. Chem. Phys.* **1978**, *68*, 5537–5562.
- (55) Erling, P. A.; Nelson, W. H. *J. Phys. Chem. A* **2004**, *108*, 7591–7595.
- (56) Pauwels, E.; Declerck, R.; Van Speybroeck, V.; Waroquier, M. *Radiat. Res.* **2008**, *169*, 8–18.

JP909247Z